

Further applications and a fully automated version of this technology are in progress.

#### ACKNOWLEDGMENT

I thank my colleagues for reviewing the manuscript: F. E. Brown, D. A. Fay, T. N. Hopper, N. C. Jamieson, G. W. Limpert, and D. L. Tuck. I also thank B. R. Semon for word processor assistance in preparing the manuscript.

Registry No. Sulfite, 14265-45-3.

#### LITERATURE CITED

- (1) Haddad, Paul R. *J. Chromatogr.* **1989**, *482*, 267-278.
- (2) Jones, William R.; Jandik, Peter J. *J. Chromatogr. Sci.* **1989**, *27*, 449-455.

- (3) Villaseñor, Steven R. Unpublished results.
- (4) Kim, Hie-Joon *J. Assoc. Off. Anal. Chem.* **1990**, *73*, 216-222.
- (5) Wagner, Herbert P.; McGarrity, Micheal J. International Ion Chromatography Symposium, San Diego, CA, 1990; *J. Chromatogr.* **1991**, *546*, 119-124 and references cited within. Authors' address: John Labatt Limited, Brewing Research Department, 150 Simcoe St, London, Ontario, Canada N6A 4M3.
- (6) Lessard, D.; Nicoll-Griffith, D.; Hill, H. M. *Am. Lab.* **1990**, *22*, 42-48.

RECEIVED for review December 13, 1990. Accepted April 5, 1991. This work was presented at the 1990 International Ion Chromatography Symposium in San Diego, CA. Permission to publish and all funding of this work was granted by Mallinckrodt Specialty Chemicals Company.

## Particle Size Distribution by Sedimentation/Steric Field-Flow Fractionation: Development of a Calibration Procedure Based on Density Compensation

J. Calvin Giddings,\* Myeong Hee Moon, P. Stephen Williams, and Marcus N. Myers

Field-Flow Fractionation Research Center, Department of Chemistry, University of Utah, Salt Lake City, Utah 84112

**Because of the important but mathematically complex role played by hydrodynamic lift forces in sedimentation/steric FFF, applied generally to particles >1  $\mu\text{m}$  in diameter, retention cannot readily be related to particle diameter on the basis of simple theory. Consequently, empirical calibration is needed. Unfortunately, retention is based on particle density as well as size so that a purely size-based calibration (e.g., with polystyrene latex standards) is not generally valid. By examining the balance between driving and lift forces, it is concluded that equal retention will be observed for equal size particles subject to equal driving forces irrespective of particle density. Therefore by adjusting the rotation rate to exactly compensate for density, retention can be brought in line with that of standards, a conclusion verified by microscopy. Linear calibration plots of log (retention time) versus log (diameter) can then be used. This approach is applied to two glass bead samples (5-30 and 5-50  $\mu\text{m}$ ) using both a conventional and a pinched inlet channel. The resulting size distribution curves are self consistent and in good agreement with results obtained independently.**

Field-flow fractionation (FFF) consists of a great number of operating modes and subtechniques, each having its own unique characteristics and range of applicability (1-3). For example, the normal mode of FFF, whether the applied field is sedimentation, thermal, crossflow, or electrical, is applicable to macromolecules and particles up to about 1  $\mu\text{m}$  in diameter, or in special circumstances up to 3 or 4  $\mu\text{m}$  particle size. The dependence of retention on particle size or mass in the normal mode is generally quite predictable, providing the force exerted on the sample particles by the applied field is a calculable quantity (2). In the normal mode of sedimentation FFF, for example, the retention time can be calculated with reasonable accuracy from first principles for particles of known size and density (4). Thus particle size distributions can be obtained

from experimental fractograms (detector response vs time curves) on the basis of theoretical relationships without recourse to the use of calibration standards. (In the normal mode of thermal FFF, some calibration is necessary simply because theoretical relationships do not exist that accurately describe the effective force exerted on polymer molecules or particles by an applied temperature gradient.)

The steric mode of operation of FFF, in contrast to normal FFF, does not yield unknown particle diameters unless subjected to empirical calibration, even if the applied force acting on the particles can be calculated (5). The reason calibration is needed is that the relatively large (over 1  $\mu\text{m}$  in diameter) particles subject to steric FFF are substantially influenced by hydrodynamic effects, particularly by hydrodynamic lift forces that tend to drive the particles away from the wall at which they normally accumulate (3). By altering the particle-wall distance in the FFF channel, these forces disturb the particle migration rate. While hydrodynamic lift forces have been studied at great length by many investigators (6-14), at the present time there are no simple yet general theoretical expressions that predict the magnitude of these forces as a function of particle diameter, shear rate, and the distance of the particle from the accumulation wall. Thus particle retention cannot be directly calculated when lift forces are substantial.

Even though calibration is clearly necessary in steric FFF, a suitable calibration procedure has not been worked out. It is the object of this report to develop such a procedure, particularly for sedimentation/steric FFF.

The first step in carrying out calibration is that of identifying suitable calibration standards. For particle sizing, the best standards (judged in terms of size range, accuracy, and narrowness of distribution) are various latex microspheres or beads. The most frequently used and widely available of these are polystyrene latex beads, which range in size from a few hundredths of a micrometer to many hundred micrometers. Many such samples can be found in the common steric range 1-100  $\mu\text{m}$ .

Our numerous experiments with both steric FFF (unpublished) and the related operating mode of hyperlayer FFF (15)

\* Corresponding author.

have shown that a plot of  $\log t_r$  vs  $\log d$  (where  $t_r$  is retention time and  $d$  is particle diameter) is approximately linear over a wide diameter range for polystyrene latex spheres. This linear relationship, or linear calibration curve, can easily be made the basis for obtaining particle size distributions from a sedimentation/steric FFF fractogram, providing the particles are polystyrene spheres or other particles of the same density.

A major difficulty, unfortunately, arises with this procedure if one attempts to obtain the particle size distribution of particles of a different chemical nature that have a different density. For such particles, the polystyrene calibration curves are no longer applicable because retention time is a function of density as well as size. Thus in some of our early experiments in steric FFF, polystyrene latex beads (density  $\rho_p = 1.05$  g/mL) and microporous silica spheres (density  $\approx 2.1$  g/mL) of almost identical diameters (5.7 vs 5.6  $\mu\text{m}$ ) were observed to have such a major difference in retention times (almost 2-fold) under the same experimental conditions that they could be essentially baseline-resolved (16). This result shows clearly that particles of one density cannot be used as calibration standards for particles of another density under the same experimental conditions in sedimentation/steric FFF. Unfortunately, because of the complexities of theory, there is no simple way to extrapolate from one density to another.

Despite the impracticality of directly applying the results obtained for a standard of one density to a sample of another density, we have developed a density compensation procedure that can be utilized to transfer results from a calibration standard to particles of other known densities.

The principles on which this procedure is based are as follows. Particles undergoing steric FFF migration are subject to two opposing forces, the primary (or applied) driving force arising from the application of the field, tending to drive the particles toward the accumulation wall, and hydrodynamic lift forces that act to drive particles away from the accumulation wall. Because of the thinness of the channel, each particle is expected to reach equilibrium rapidly. The equilibrium position will be located a short distance above the accumulation wall, where the two forces exactly balance one another (3). We know from previous experiments that if the primary driving force is increased, the particles are driven closer to the accumulation wall, whereas if it is decreased, the particles seek an equilibrium position further from the wall (3, 16). This is confirmed by the fact that the retention time is increased and decreased by these two respective changes. As long as the primary driving force is unchanged and other experimental conditions are the same, the particles will migrate along the channel at a fixed equilibrium height and a fixed velocity. All identical particles migrate at the same velocity and emerge with the same retention time because they are subject to the same primary driving force.

If now we introduce into a sedimentation FFF system a particle of the same size but one that is different in density, it will migrate at a different velocity because the primary driving force, sedimentation, varies with particle density. However, the particle of different density can be made to migrate at the same velocity providing we somehow compensate for the density change in such a way that the primary driving force stays the same. This is accomplished in our procedure by changing the field strength (specifically, the rotation rate) of the centrifuge so that the density change is exactly offset by the rpm change. With such compensation, the primary driving force remains unchanged.

More specifically, the driving force of sedimentation is directly proportional to the density difference  $\Delta\rho$  between the particle and its surrounding carrier liquid. This force is also proportional to acceleration  $G$  or, equivalently, to  $\text{rpm}^2$ . Thus when sample particles having a density different from that

of the standard particles are used, the calibration curve for the standards can be utilized, providing  $G$  for the sample is varied inversely with its  $\Delta\rho$ ,  $G = (\text{constant})/\Delta\rho$ , with all other conditions including flow velocity remaining the same. (This procedure is based on the reasonable assumption that lift forces are independent of particle density.) Equivalently, this density compensation can be realized if the rotation rate varies as  $\text{rpm} = (\text{constant})/(\Delta\rho)^{1/2}$ . Clearly, the method is applicable only to samples in which all particles have the same density and thus the same  $\Delta\rho$ .

The calibration procedure based on this density compensation effect thus proceeds as follows. First, a calibration curve relating  $t_r$  to  $d$  is established using well-characterized standards under appropriate conditions. (The calibration curve may involve a plot of  $\log t_r$  vs  $\log d$ , or it may employ any other graphical, analytical, or numerical relationship between  $t_r$  and  $d$ .) Second, the sample of interest is run with all conditions the same except that  $G$  is adjusted according to the relationship  $G = (\text{constant})/\Delta\rho$ , as explained above. Third, standard procedures and their modifications (see below) can then be used to obtain the particle size distribution.

By compensating for density differences by means of carefully chosen adjustments in field strength or rpm, one can use the most convenient particle size standards regardless of their density. This compensation procedure allows one to bypass the difficulties of the complex theoretical treatments needed (but not yet developed) to relate retention time to particle size and density in steric FFF.

## THEORY

The particle size distribution  $m(d)$ , expressing the relative mass  $m$  of particulate matter lying in a unit range of particle diameter  $d$ , is obtained from the equation (17)

$$m(d) = c(t_r) \left| \frac{dV_r}{dd} \right| \quad (1)$$

where  $c(t_r)$  is the corrected (see later) fractogram signal, proportional to the mass concentration  $c$  of particulate matter in the channel effluent emerging at retention time  $t_r$ , and  $V_r$  is the retention volume. Equation 1 can be transformed to

$$m(d) = c(t_r) \left| \frac{dV_r}{dt_r} \right| \left| \frac{dt_r}{dd} \right| = c(t_r) \bar{V} \left| \frac{dt_r}{dd} \right| \quad (2)$$

where  $\bar{V}$  represents the flow rate through the channel. The absolute value bars are used because retention times  $t_r$  or volume  $V_r$  may either increase (normal mode of FFF) or decrease (steric FFF) with  $d$  without affecting the validity of the above equations.

Equations 1 and 2 show that the particle size distribution function  $m(d)$  can only be obtained from the fractogram response function  $c(t_r)$  if the retention time  $t_r$  (or, equivalently, the retention volume  $V_r$ ) is a known function of particle diameter  $d$  so that  $dt_r/dd$  may be obtained. In normal FFF, as pointed out earlier, this dependency is generally obtained from theory; in steric FFF, the relationship between  $t_r$  and  $d$  must be obtained by empirical calibration. The precise form of this function is unimportant mathematically, and the way it is obtained is of no significance as long as a valid relationship is known so that  $dt_r/dd$  can be obtained.

As noted above, for steric FFF a plot of  $\log t_r$  vs  $\log d$  normally yields a straight line. This straight line relationship can be expressed by

$$\log t_r = -S \log d + \log t_{r1} \quad (3)$$

or, if  $t_r$  is tabulated as the dimensionless ratio  $t_r/t^\circ$  by

$$\log \frac{t_r}{t^\circ} = -S \log d + \log \frac{t_{r1}}{t^\circ} \quad (4)$$

where  $S$ , the negative slope of the plot, is equal to the particle

diameter selectivity (sometimes written as  $S_d$ ),  $|d \log t_r / d \log d|$ ,  $t^\circ$  is the void time, and  $t_{r1}$  is a constant equal to the extrapolated value of  $t_r$  for particles of unit diameter. These equations can be expressed in the alternate form

$$t_r = t_{r1}/d^S \quad (5)$$

As long as eqs 3–5 are valid, the derivative term in eq 2 becomes

$$dt_r/dd = -St_{r1}d^{-(S+1)} \quad (6)$$

When eq 6 is substituted into eq 2, we have

$$m(d) = c(t_r) \dot{V} S t_{r1} / d^{S+1} = c(t_r) \dot{V} S t_{r1} (t_r / t_{r1})^{(S+1)/S} \quad (7)$$

where the minus sign has disappeared because of the absolute value designation in eq 2. The latter expression of eq 7 can be used directly to obtain  $m(d)$  from the fractogram function  $c(t_r)$ , provided the constants  $S$  and  $t_{r1}$  are known.

We note that the signal from some detectors used in FFF (particularly detectors, such as ours, that record the level of light scattering) is not only proportional to the mass concentration  $c$  of particles per unit volume but also depends on particle size. In this instance, corrections must be applied to obtain the correct distribution function  $m(d)$  (see later).

It is inevitable that the acquired  $m(d)$  curves will be slightly broadened by band dispersion processes in the channel. However, the variance of our sample peaks is nearly 2 orders of magnitude greater than the variance of latex standard peaks, indicating that the perturbation to  $m(d)$  is negligible.

### EXPERIMENTAL SECTION

The sedimentation FFF rotor unit, similar to units utilized in previous work (18), has the same basic structure as the Model S101 colloid/particle fractionator from FFFractionation, Inc. (Salt Lake City, UT). These systems all have a horizontal spin axis (a vertical spin plane) to prevent larger particles from settling to the edges of the channel during the run due to gravitational sedimentation.

Two different channels were used in this study to verify the generality of the calibration procedure. Channel I is a conventional channel, uniform in cross section from end to end, having a tip-to-tip length  $L$  of 92 cm, a breadth  $b$  of 2 cm, and a thickness  $w$  of 254  $\mu\text{m}$ , equal to the thickness of the Mylar spacer from which the channel was cut. The void volume, measured as the elution volume of a nonretained sodium benzoate peak, is 5.1 mL. Channel II has a more novel pinched inlet design (19), in which the first 40% of the channel length is only 127  $\mu\text{m}$  thick as compared to the 254- $\mu\text{m}$  thickness of the remainder of the channel (20). This unique structure, designed for stopless flow operation (injection without stopflow), was constructed by using two 127  $\mu\text{m}$  thick sheets of Mylar plastic. The piece having the full channel dimensions,  $L = 90$  cm and  $b = 2$  cm, was cut and removed from one of the sheets. The other sheet was cut in such a way that a "blocking element" was left in place along 36 cm of the inlet end. The blocking element was layered against the inside channel wall, as shown in Figure 1. The void volume of the pinched inlet structure, measured as before, is 3.6 mL.

The standards used for calibration are polystyrene latex beads (Duke Scientific, Palo Alto, CA) with reported diameters of 59.7, 47.9, 29.1, 19.58, 15.0, 9.87, 7.04, 5.002, 3.983, and 2.062  $\mu\text{m}$  (hereafter described as 60, 48, 29, 20, 15, 10, 7, 5, 4, and 2  $\mu\text{m}$ , respectively). Two polydisperse glass bead samples were used to test our calibration procedure for size characterization. A nominal 5–50- $\mu\text{m}$  material from Duke Scientific and a 5–30- $\mu\text{m}$  sample from the National Institute of Standards and Technology (NIST) (SRM 1003) were used. The glass bead samples were treated with a density flotation method to rid them of beads containing bubbles. This density fractionation was achieved by using 1,4-diiodobutane with a density of 2.35 g/mL. The resulting high-density glass bead samples were cleaned with ethyl alcohol and the aqueous carrier several times. Sample volumes of 70–80  $\mu\text{L}$  of well-stirred 35 mg/mL glass bead suspensions were injected for each run. For channel I, the sample was injected directly into the channel inlet by a microsyringe. The carrier flow was then

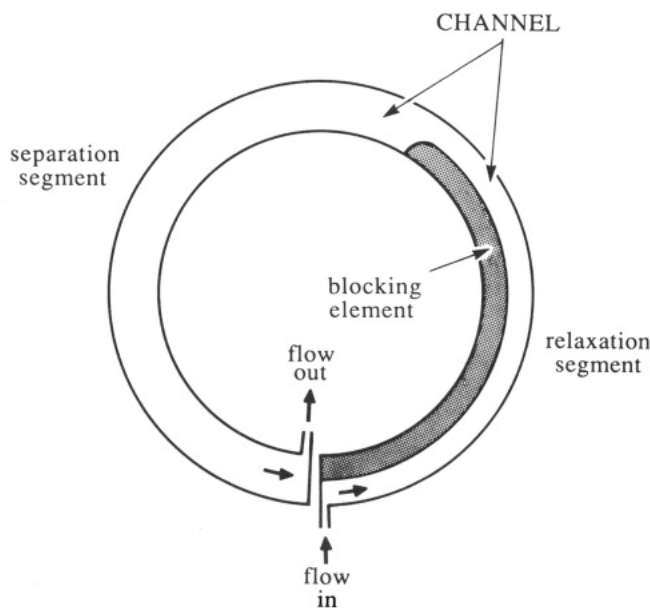


Figure 1. Schematic diagram of structure of pinched inlet channel (channel II) for sedimentation FFF.

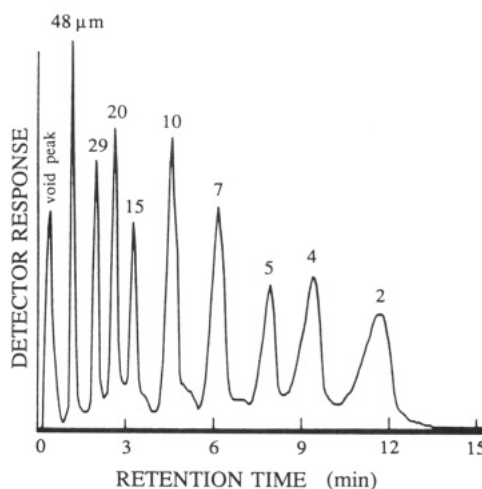
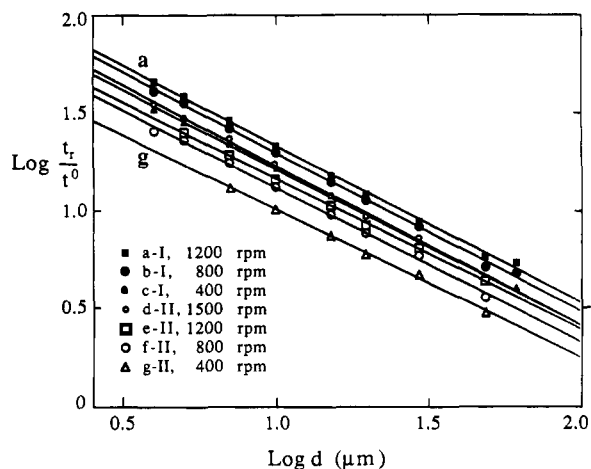


Figure 2. Separation of nine polystyrene latex standards of the indicated diameters in the pinched inlet channel at 800 rpm and  $\dot{V} = 10.3$  mL/min.

interrupted (following the stopflow procedure) and the centrifuge set spinning to achieve sample relaxation. Flow was then resumed. For channel II, whose structure is designed to make the stopflow procedure unnecessary (19), the channel was first brought up to its final rotational speed and the sample was introduced into the continuously flowing stream entering through the inlet tubing and seal.

The carrier liquid used for these experiments was doubly distilled water with 0.01% FL-70 detergent (Fisher Scientific Co., Fairlawn, NJ) used for particle stabilization and 0.02% sodium azide used as bactericide. The carrier flow was driven by an FMI Lab pump Model QD-2 (Fluid Meeting, Inc., Oysterbay, NJ).

The eluted sample was monitored at 254 nm by an Altex Model 153 (Beckman Instrument, Fullerton, CA) UV detector. A strip chart recorder from Houston Instrument Corp. (Austin, TX) was used for recording. Particle fractions were collected on a Model FC-80K microfractionator from Gilson Medical Electronics (Middletown, WI). These samples were then examined by microscopy. Calibration curves were established by measuring the retention times of each of a series of latex beads under specified conditions. Retention times can be accurately measured because latex microspheres of different diameters form sharp peaks, as illustrated in Figure 2. This fractogram, obtained by running a sample consisting of a mixture of the nine latex standards of different diameters used in this study in Channel II, illustrates the high resolution that can be achieved in particle size analysis



**Figure 3.** Least-squares linear calibration curves for polystyrene latex standards obtained at a flow rate of 10.3 mL/min. The nine sets of experimental points along the  $\log d$  axis are obtained for latex microspheres of diameter 4, 5, 7, 10, 15, 20, 29, 48, and 60  $\mu\text{m}$ , respectively. The top three plots (a–c) are for channel I and the four plots below (d–g) apply to channel II. The rpm for each plot is shown in the diagram and in Table I. The slope and intercept parameters are given in Table I.

**Table I. Experimental Conditions and Parameters Corresponding to Calibration Plots of Figure 3<sup>a</sup>**

plot	channel	rpm	$G\Delta\rho \times 10^{-4}$ , $\text{g}/(\text{cm}^2 \text{s}^2)$	$S$	$t_{r1}/t_0$	$cc^b$
a	I	1200	1.244	0.813	140.6	0.998
b	I	800	0.553	0.823	132.4	0.998
c	I	400	0.138	0.812	106.4	0.998
d	II	1500	1.943	0.824	113.5	0.998
e	II	1200	1.244	0.780	88.3	0.999
f	II	800	0.553	0.796	82.2	0.998
g	II	400	0.138	0.764	58.9	0.998

<sup>a</sup>All flow rates = 10.3 mL/min. <sup>b</sup>Correlation coefficient for plot.

using sedimentation/steric FFF.

## RESULTS AND DISCUSSION

A series of seven calibration plots is shown in Figure 3. The plots correspond to different rotation rates applied to the two different channel systems, as specified in Table I. All runs were made at a flow rate of 10.3 mL/min. The straight lines shown in the figure were obtained by least squares. The slope ( $-S$ ) and intercept ( $t_{r1}/t_0$ ) are also shown in Table I.

The plots displayed in Figure 3 (and tabulated in Table I) consist only of the linear portions of the logarithmic time-diameter relationship corresponding to fully developed steric FFF. As one proceeds left along any given plot (in the direction of smaller particle diameter), the steric transition region is encountered. As one proceeds into this region, Brownian motion, which dominates the normal operating mode of FFF, plays an increasing role in driving particles away from the accumulation wall. This effect leads to earlier elution than would be expected on the basis of steric effects alone. Therefore, the plots begin to bend downward (toward shorter retention times) upon proceeding through the steric region, eventually passing through a maximum at the steric transition point (see Figure 4). The retention of particles of still smaller diameter is governed largely by normal FFF, but a significant steric influence persists well beyond the transition point.

While the plots of Figure 3 and the theory culminating in eq 7 focus on the straight line portion of the logarithmic plots, the density compensation principle can be extended through the entire steric transition region and, if necessary, into the domain of normal FFF. This is because both steric and normal FFF, other forces being equal, are governed by the magnitude

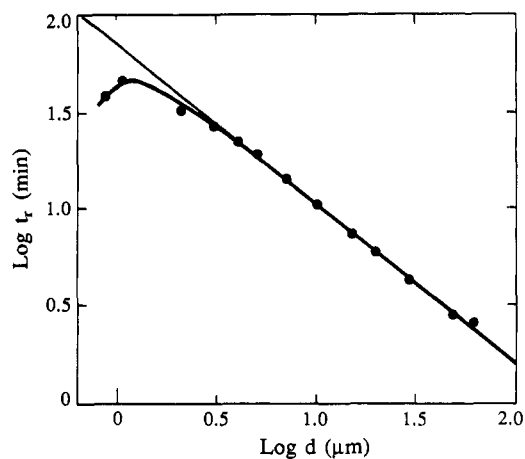


**Figure 4.** Calibration plot that shows extension of plot a in Figure 3 (channel I) into curved steric transition region for small  $d$ .

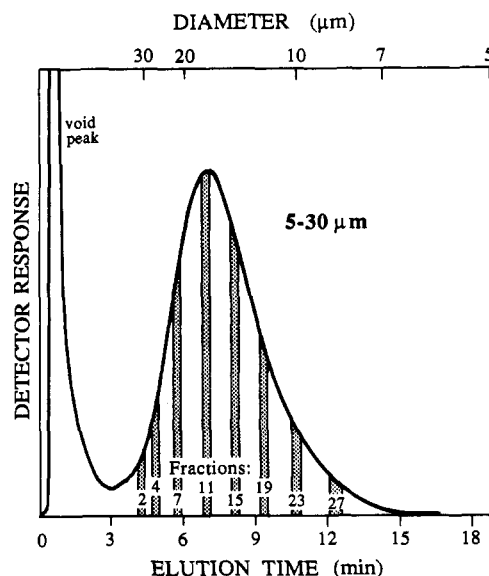


**Figure 5.** Fractogram of polydisperse 5–30- $\mu\text{m}$  glass bead sample in channel I at 224 rpm, a flow rate of 10.3 mL/min, and a stopflow time of 2 s.

of the primary driving force, which is reduced to a common level by means of the compensation procedure. While particle diameters in normal FFF can be approximately related to retention time by theory, as noted earlier, perturbations caused by steric effects, and even by electrostatic and related forces, can be corrected by density compensation, provided the distributing forces are the same for particles of equal size independent of particle density.

While the validity of eq 7 fails to extend into the steric transition region because eq 3, on which eq 7 is based, no longer applies, the general relationships provided by eqs 1 and 2 are applicable over the entire particle diameter range, including that corresponding to steric FFF, normal FFF, and the transition region. (These equations become momentarily inoperable right at the transition point because  $dt_r/dd$  and thus selectivity  $S$  equal zero at this point.) It is only necessary to replace eq 3 by a more appropriate relationship to extend eqs 1 and 2 into the transition region and beyond.

Figures 5 and 6 show fractograms of the two polydisperse glass bead samples with nominal diameter ranges of 5–30 and 5–50  $\mu\text{m}$ , respectively. Both fractograms were obtained with the uniform channel, channel I, at a flow rate of 10.3 mL/min and with a stopflow time of 2 s. The 5–30- $\mu\text{m}$  sample, having a density of 2.41 g/mL, was run at a rotation rate of 224 rpm. Under these conditions, the  $G\Delta\rho$  value is exactly the same as

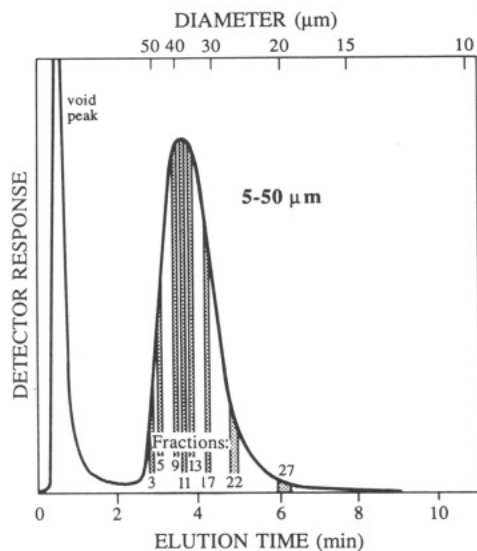


Figure 6. Fractogram of 5–50- $\mu\text{m}$  glass bead sample in channel I at 222 rpm,  $\dot{V} = 10.3$  mL/min, and a stopflow time of 2 s.

that applicable to the polystyrene latex standards represented by line a (1200 rpm) in Figure 3. Since the latter plot fixes a relationship between retention time and particle diameter that under these specific conditions presumably applies to the glass bead sample, a particle diameter scale can be readily applied to Figure 5, as shown along the upper horizontal axis. This scale verifies that most of the glass spheres fall in the range 5–30  $\mu\text{m}$  as specified by the supplier.

The fractogram (Figure 6) of the 5–50- $\mu\text{m}$  sample (density 2.45 g/mL) was obtained at 222 rpm. The  $G\Delta\rho$  value here also corresponds very closely to plot a in Figure 3. The diameter scale obtained from the calibration plot is again shown on the upper horizontal axis. Based on this scale, it appears that most of the spheres have diameters from 20–50  $\mu\text{m}$  with only a minor part of the population having a diameter less than 15  $\mu\text{m}$ .

Fractions were collected from the elution stream in both of the above runs in order to examine the bead diameters microscopically and test the validity of our method. More than 30 fractions were collected for each sample, and a detailed microscopic examination was carried out on these. Results are reported here for about one-third of the fractions (Table II). The positions of the reported fractions are shown in the fractograms of Figures 5 and 6 and identified by a fraction number. Table II tabulates the microscopically determined mean diameters (based on a count of from 20 to 30 spheres for each fraction) and compares these to the diameters based on the proposed calibration procedure. The agreement is seen to be excellent, thus confirming in large measure the validity of the density compensation approach to calibration.

The fractionation of glass microspheres according to size is illustrated in Figure 7, which shows micrographs of the original 5–50- $\mu\text{m}$  sample and a number of the fractions collected at positions along the time axis indicated in Figure 6. As expected, the larger particles are eluted in the earlier fractions. Some of these particles show residual bubbles despite the flotation process used in sample preparation.

Given the correctness of the calibration relationship relating retention time to particle diameter as confirmed by the microscopy reported above, we are in a position to convert the fractograms such as those shown in Figures 5 and 6 into particle size distribution (PSD) curves. For this purpose, eq 7 is used along with software developed in-house. This treatment converts the fractogram of Figure 5 into the size distribution curves shown in Figure 8. If the response curve of the fractogram in Figure 5 directly replaces  $c(t_r)$  in eq 7,

Table II. Comparison of Glass Bead Diameters of Collected Fractions Based on Calibration Procedure and on Microscopy

fraction	time, min	diameter based on calibration, $\mu\text{m}$	diameter based on micrograph, $\mu\text{m}$
A. Fractions from 5–30- $\mu\text{m}$ Sample (Figure 5)			
2	4.10–4.40	32.6–29.9	32.5 $\pm$ 1.7
4	4.70–5.00	27.6–25.5	24.9 $\pm$ 3.0
7	5.60–5.90	22.2–20.8	21.0 $\pm$ 1.3
11	6.80–7.10	17.5–16.6	17.5 $\pm$ 1.1
15	8.00–8.30	14.3–13.7	13.6 $\pm$ 1.2
19	9.20–9.50	12.1–11.6	11.7 $\pm$ 0.7
23	10.50–10.90	10.3–9.8	9.7 $\pm$ 1.1
27	12.10–12.60	8.6–8.2	8.4 $\pm$ 0.8
B. Fractions from 5–50- $\mu\text{m}$ Sample (Figure 6)			
3	2.80–2.90	52.1–49.9	51.9 $\pm$ 0.2
5	3.00–3.10	47.9–46.0	47.1 $\pm$ 1.8
9	3.40–3.50	41.0–39.6	41.5 $\pm$ 2.5
11	3.60–3.70	38.3–37.0	38.4 $\pm$ 2.1
13	3.80–3.90	35.8–34.7	36.9 $\pm$ 2.6
17	4.20–4.30	31.7–30.7	31.3 $\pm$ 1.7
22	4.80–5.00	26.9–25.5	24.9 $\pm$ 1.9
27	6.00–6.30	20.4–19.6	18.6 $\pm$ 1.4
33	8.30–8.70	13.7–12.9	13.5 $\pm$ 0.5

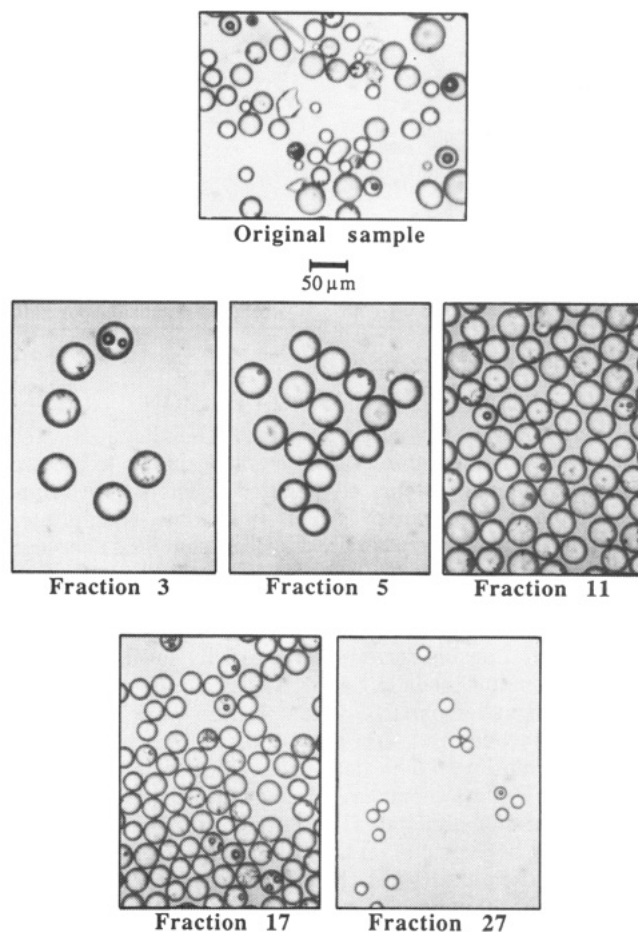


Figure 7. Optical micrographs of original 5–50- $\mu\text{m}$  glass bead sample and of various fractions collected from the eluting stream at the time intervals shown in Figure 6. The detailed results of the microscopic examination of fractions are provided in Table II.

the center PSD curve of Figure 8 emerges. However, as noted earlier,  $c(t_r)$  must be corrected if the detector signal, as in our case, depends on particle diameter as well as sample amount. Since the signal from our detector originates in scattered light, it is roughly proportional to the surface area of particles (such

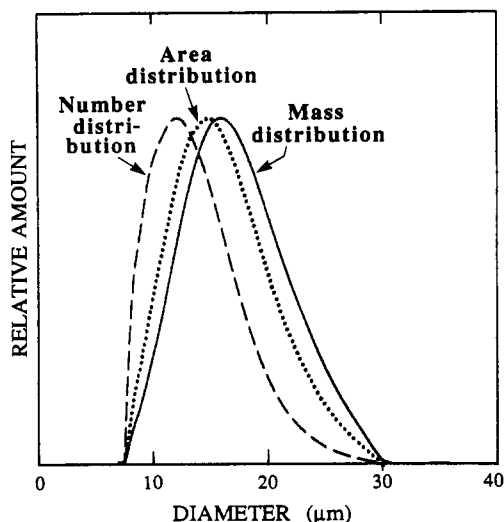


Figure 8. Number, area, and mass distribution curves obtained for the 5–30- $\mu\text{m}$  glass bead sample by using the fractogram shown in Figure 5.

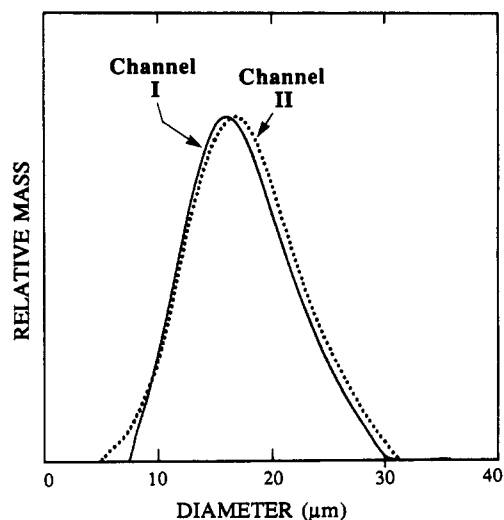


Figure 9. Comparison of mass-based size distribution curves for 5–30- $\mu\text{m}$  glass bead sample (SRM 1003) using channels I (uniform) and II (pinched).

as ours) whose diameters greatly exceed the wavelength (254 nm) of the incident light beam. Thus the uncorrected center curve can be interpreted as a surface area-weighted size distribution curve. When  $c(t_r)$  in eq 7 is obtained by multiplying the signal by particle diameter  $d$ , a true mass distribution curve is produced, as shown by the right-hand curve of Figure 8. On the other hand, if the signal is divided by  $d^2$ , the number distribution curve shown to the left side of Figure 8 is generated. In subsequent figures we will show only mass-based size distribution curves.

A critical test of our calibration procedure that complements microscopy entails a comparison of particle size distribution (PSD) curves obtained from different channels, such as channels I and II, that differ significantly in structure (uniform versus pinched inlet) and operation (stopflow procedure versus stopless flow injection). Both channels, of course, must be separately calibrated with latex beads, as done here. Once  $S$  and  $t_{r1}$  are obtained by calibration and  $G$  is adjusted for density compensation, the size distribution can be obtained from the observed fractogram by using eq 7.

Figure 9 shows the two PSD curves obtained for the 5–30- $\mu\text{m}$  glass bead sample by using the two different channels I and II. The calibration plots and parameters for these two cases are shown in Figure 3 and Table I as plots a and e for

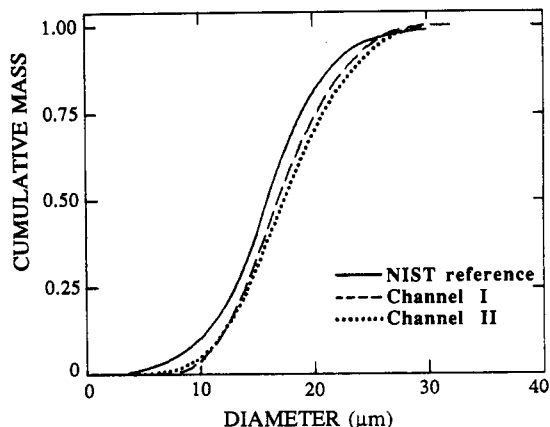


Figure 10. Comparison of cumulative size distribution curves obtained from the two FFF channels and a reference curve obtained from NIST.

the two respective channels. (The input fractogram for the channel I PSD is shown in Figure 5). These two PSD curves are in basic agreement in support of lower and upper cutoff diameters of approximately 5 and 30  $\mu\text{m}$ , respectively, for the sample. They differ by about 1  $\mu\text{m}$  on the diameter of the peak of the distribution, which appears to lie in the vicinity of 15 or 16  $\mu\text{m}$ . Overall, the agreement of the two PSD curves is very good.

The size distribution given by NIST for this standard reference material (SRM 1003) is presented in cumulative form. When the size distribution curves of Figure 9 are converted to cumulative form and plotted against the NIST reference curve, the three close-lying cumulative distributions shown in Figure 10 are obtained. Although the agreement is satisfactory, the NIST reference curve displays diameters from 1 to 2  $\mu\text{m}$  smaller than those obtained from the FFF curves for fixed values of the cumulative mass. (For example, at 50% cumulative mass, the NIST diameter is 15.8  $\mu\text{m}$  while the Channel I diameter is 17.0  $\mu\text{m}$ ). This discrepancy, although not major, is not supported by the microscopy results reported in Table II, which show very good overall agreement with the calibration diameters. Some of the difference relative to the NIST curve could be due to the removal of much of the gas-void population, which might shift the PSD of the remaining bead population. However, incomplete removal (as we observe) is probably worse because the gas inclusions will reduce bead density and lead to early elution, in which case they are counted as larger particles. Clearly, our methodology works imperfectly for particles that are heterogeneous in density like the present glass bead populations.

Some error in the PSD may also be introduced by imperfect sampling techniques since proper sampling is difficult in this size range. However, preliminary experiments involving variations in sampling procedures suggest that the sampling error is  $<1 \mu\text{m}$ .

We note that without the density-compensated calibration developed here, the particle diameter at the 50% cumulative point would be shifted from 17.0 to 8.8  $\mu\text{m}$ . The latter value is unacceptably low, demonstrating that density effects must be properly accounted for.

Figure 11 compares the PSD's obtained for the nominal 5–50- $\mu\text{m}$  sample by using channels I and II. The agreement with the reported 5- $\mu\text{m}$  lower limit is not as good as that shown in Figure 8; this may be due to a very small (perhaps negligible) population of 5–10- $\mu\text{m}$  beads, observed microscopically, that are lost in our baseline.

## CONCLUSIONS

Although retention in sedimentation/steric FFF is not fully described by theory, particle size distribution curves can be obtained by constructing  $\log t_r$  versus  $\log d$  calibration plots

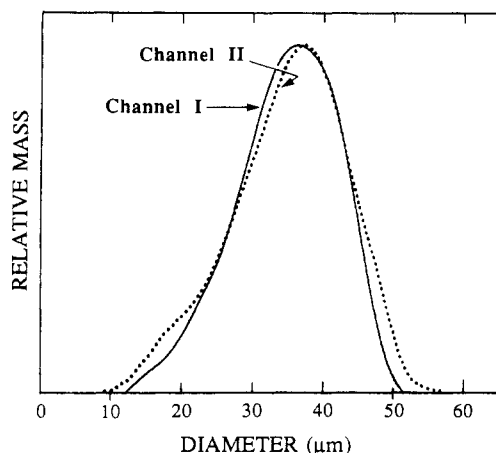


**Figure 11.** Comparison of mass-based size distribution curves for the 5–50- $\mu\text{m}$  sample obtained from channels I and II.

using polystyrene latex beads and then by changing the rotation rate of the centrifuge to compensate for the density difference between the sample material and the latex calibrant. This procedure is shown to yield good results when tested by (a) microscopy, (b) self-consistency between two different FFF channel structures, and (c) a comparison with an external (NIST) cumulative size distribution curve. Further refinements in this approach should lead to increased speed and accuracy.

#### GLOSSARY

$b$	channel breadth
$c$	mass concentration in effluent
$c(t_r)$	corrected fractogram signal
$d$	particle diameter
$G$	acceleration
$L$	channel length
$m$	particle mass

$m(d)$	particle size distribution function
$S$	particle diameter selectivity ( $=S_d$ )
$t^0$	void time
$t_r$	retention time
$t_{r,1}$	retention time for particles of unit diameter
$V$	flow rate through channel
$V_r$	retention volume
$w$	channel thickness

#### Greek Alphabet

$\Delta\rho$	density difference between particle and carrier
$\rho$	particle density

#### LITERATURE CITED

- Giddings, J. C. *Anal. Chem.* **1981**, *53*, 1170A–1175A.
- Giddings, J. C. *Sep. Sci. Technol.* **1984**, *19*, 831–847.
- Giddings, J. C.; Chen, X.; Wahlund, K.-G.; Myers, M. N. *Anal. Chem.* **1987**, *59*, 1957–1962.
- Karaiskakis, G.; Myers, M. N.; Caldwell, K. D.; Giddings, J. C. *Anal. Chem.* **1981**, *53*, 1314–1317.
- Peterson, R. E., II; Myers, M. N.; Giddings, J. C. *Sep. Sci. Technol.* **1984**, *19*, 307–319.
- Segré, G.; Silberberg, A. *Nature* **1961**, *189*, 209–210.
- Segré, G.; Silberberg, A. *J. Fluid Mech.* **1962**, *14*, 115–135.
- Segré, G.; Silberberg, A. *J. Fluid Mech.* **1962**, *14*, 136–157.
- Saffman, P. G. *J. Fluid Mech.* **1965**, *22*, 385–400.
- Cox, R. G.; Brenner, H. *Chem. Eng. Sci.* **1968**, *23*, 147–173.
- Ho, B. P.; Leal, L. G. *J. Fluid Mech.* **1974**, *65*, 365–400.
- Vasseur, P.; Cox, R. G. *J. Fluid Mech.* **1976**, *78*, 385–413.
- Cox, R. G.; Hsu, S. K. *Int. J. Multiphase Flow* **1977**, *3*, 201–222.
- Leal, L. G. *Annu. Rev. Fluid Mech.* **1980**, *12*, 435–476.
- Ratanathanawongs, S. K.; Giddings, J. C. *J. Chromatogr.* **1989**, *467*, 341–356.
- Caldwell, K. D.; Nguyen, T. T.; Myers, M. N.; Giddings, J. C. *Sep. Sci. Technol.* **1979**, *14*, 935–946.
- Giddings, J. C.; Myers, M. N.; Yang, F. J. F.; Smith, L. K. In *Colloid and Interface Science*; Kerker, M., Ed.; Academic Press: New York, 1976; Vol. IV, pp. 381–398.
- Koch, T.; Giddings, J. C. *Anal. Chem.* **1986**, *58*, 994–997.
- Giddings, J. C. *Sep. Sci. Technol.* **1989**, *24*, 755–768.
- Moon, M. H.; Myers, M. N.; Giddings, J. C. *J. Chromatogr.* **1990**, *517*, 423–433.

RECEIVED for review December 17, 1990. Accepted April 16, 1991. This work was supported by Public Health Service Grant GM10851-33 from the National Institutes of Health.

## Nanoliter-Scale Multireflection Cell for Absorption Detection in Capillary Electrophoresis

Tiansong Wang, Joseph H. Aiken, Carmen W. Huie, and Richard A. Hartwick\*

Department of Chemistry, State University of New York at Binghamton, Binghamton, New York 13902

**A multireflective absorption cell for CZE is fabricated and examined by both static and dynamic measurements. The new cell is characterized by improved sensitivity as compared to conventional single-pass cells, with no increase in cell volume. A 40-fold improvement in sensitivity is obtained when compared to a single-pass cell, with similar noise levels. A concentration detection limit of  $6.5 \times 10^{-8}$  M for brilliant green is estimated for the new cell design from static measurements. A theoretical analysis of cell performance using ray tracing for both axial and radial reflections in the new cell shows good agreement with experimental results.**

#### INTRODUCTION

Detection is one of most important and rapidly developing areas in capillary zone electrophoresis (CZE). Various detection principles, such as spectrophotometric, mass spectrometric, electrochemical, and radiometric detection, have

been applied to CZE (1). Although the sensitivity of UV-visible absorption detection is perhaps the lowest among these detection methods, UV detectors are the most popular detector currently utilized in CZE because of their simplicity and versatility.

Most UV detectors in CZE employ single-pass detection, which was first introduced by Yang for capillary liquid chromatography (2). In this design, the light beam travels normal to the capillary axis, crossing the capillary only a single time. According to Beer's law,

$$A = \epsilon bc \quad (1)$$

where  $A$  is the absorbance,  $\epsilon$  is the molar extinction coefficient of the sample,  $b$  is the light path length, and  $c$  is the sample concentration. The low sensitivity in single-pass detection is predictable because the path length is limited by the inner diameter of the capillary, typically 50–75  $\mu\text{m}$ . Therefore, even with state of the art detectors, concentration detection limits are rarely lower than ca.  $10^{-6}$  M.